A Chemical Route to $Yb_{14}MgSb_{11}$ Composites with Nano-Sized Iron Inclusions for Reduction of Thermal Conductivity

Christopher J. Perez,[1] Zhijie Chen,[2] Willie B. Beeson,[2] Sevan Chanakian,[3] Kai Liu,[2] Sabah K. Bux,[3*] and Susan M. Kauzlarich[1*]

[1] Department of Chemistry, University of California, One Shields Avenue, Davis, CA 95616, USA.

[2] Physics Department, Georgetown University, 37th and O Sts. NW, Washington, DC 20057, USA.

[3] Thermal Energy Conversion Research and Advancement Group, Jet Propulsion Laboratory, California Institute of Technology, 4800 Oak Grove Dr., Pasadena, CA 91109-8099, USA.

Keywords: Thermoelectric, Composite, Binary precursor, Transport properties, Zintl phase.

* Corresponding authors: sabah.k.bux@jpl.nasa.gov, smkauzlarich@ucdavis.edu

---

Abstract

The rapid rise of atmospheric CO_2 has spurred keen research interests in sustainable energy technologies including thermoelectric materials which can reliably and robustly turn heat directly to electricity. $Yb_{14}MnSb_{11}$ has been the material of intense study because of its high thermoelectric figure of merit, *zT*. A structural analog, $Yb_{14}MgSb_{11}$, is also of interest as it has a higher average zT ($\int_{T_c}^{T_h} Z(T)dT, ZT$) and a comparable peak *zT* (1.3 vs 1.2) to $Yb_{14}MnSb_{11}$. We have shown that $Yb_{14}MgSb_{11}$ can be composited with micron sized iron particles with significant improvements to the thermoelectric Power Factor and mechanical properties. In this work we successfully employ a rapid high temperature *in situ* reaction to create well dispersed nanoscale (<100 nm) iron inclusions in the bulk $Yb_{14}MgSb_{11}$ matrix *via* the decomposition of $FeSb_2$ into Fe and Sb. The incorporation of nanoscale iron into $Yb_{14}MgSb_{11}$ further reduces lattice thermal conductivity (κ_l), when compared to the previously published micron iron composites, due to an increase in phonon scattering. As a result of the synchronous decrease in thermal conductivity and resistivity the 7.3 vol% Fe sample retains the *zT* of $Yb_{14}MgSb_{11}$ while achieving a 43% Power Factor improvement.

1. Introduction

Thermoelectric generators have been explored as sustainable energy conversion devices that can synergistically supplement power generators such as the internal combustion engine and solar girds or can operate as stand-alone generators in remote locations such as outer space.[1-3] In addition, they have great potential to be incorporated into internet of things (IoT) technologies such as garments with sensors powered by thermoelectric generators that can gather biometric data.[4-6] Thermoelectric generators are heat engines where electrons are the working fluid comprised of *n*-type and *p*-type materials linked thermally in parallel and electrically in series.[7-8] The efficiency of a thermoelectric generator is a function of the Carnot efficiency (η) and *ZT*, which is the material's thermoelectric figure of merit, *zT*, integrated over an operational temperature range (see equations (1), (2), (3), respectively), where: $\mathrm{S} =$ Seebeck coefficient $\left(\frac{\mathrm{V}}{\mathrm{K}}\right)$, $\mathrm{T} =$ absolute temperature (K), $\rho =$ electrical resistivity (Ωm), and κ_{tot} is the total thermal conductivity generally decomposed into its electronic, κ_e, and lattice, κ_l, components.

Of the high temperature (873 – 1273 K) *p*-type materials, the structurally complex $Yb_{14}MnSb_{11}$ phase is one of the best with $zT = 1.3$ at 1227 K due to a large Seebeck coefficient and extremely low thermal conductivity.[9] Strategies for improving the *zT* of $Yb_{14}MnSb_{11}$ have either focused on optimizing the Seebeck term which is derived from the electronic structure, thereby maximizing the Power Factor (*PF*) (eq. 4), or reducing the lattice thermal conductivity, κ_l, the only parameter that is not directly related to the carrier concentration.[10-13] Electronic tuning of $Yb_{14}MnSb_{11}$ has been achieved by alloying with Al,[14] La,[15] Pr, Sm,[16] Sc, Y,[17] Ca,[18] Te,[19] and Zn,[20] to identify a few.[21] The most successful in terms of increasing *zT* has been the solid solution containing Al, $Yb_{14}Mn_{1-x}Al_xSb_{11}$ (x = 0.6, 0.8).[14] Analogs of the structure type such as $Yb_{14}MgSb_{11}$ with a max *zT*s of 1.2 can also provide new compositions for optimization.[22-23] $Yb_{14}MgSb_{11}$ is an exciting phase because it has a higher Seebeck coefficient than $Yb_{14}MnSb_{11}$, and has a higher *ZT* (see equation (2)) at 873-1273 K (1.10 vs 1.07).[9, 24-25]

$$\eta = \frac{T_h - T_c}{T_h}\left(\frac{\sqrt{1+ZT}-1}{\sqrt{1+ZT}+\frac{T_c}{T_h}}\right) \quad (1), \qquad ZT = \frac{1}{\Delta T}\int_{\mathrm{T_c}}^{\mathrm{T_h}} \mathrm{Z(T)\,dT} \quad (2),$$

$$zT = \frac{\mathrm{S^2T}}{\kappa_{\mathrm{tot}}\rho} \quad (3), \qquad PF = \frac{S^2}{\rho} \quad (4).$$

Reducing κ_l has long been a strategy for improving zT. One method of reducing κ_l is alloy scattering where atoms with large mass discrepancies are substituted into a structure such as alloying $Yb_{14}MnSb_{11}$ with Ca causing a significant reduction in thermal conductivity.[18, 26] Additional methods to reduce κ_l include nanostructuring and compositing. Nanostructuring involves controlling the grain size of a material to be smaller than the phonon mean free path, leading to phonon scattering and a reduction in κ_l.[10, 27-28] This strategy is demonstrated for $Bi_xSb_{2-x}Te_3$ where orienting nanoplates led to peak zTs of 1.83 due to a large reduction in thermal conductivity.[29] A nanocomposite results from introducing nano-sized inclusions of a phase dispersed in a bulk medium and has been known to increase zT through a variety of mechanisms. Nanocomposites of the phases, Bi_2Te_3, PbTe, PbSe, PbS, $AgSbTe_2$, Skutterudites, and half-Heuslers, have been shown to effectively reduce κ_l and have the potential to strengthen the bulk mechanical properties, which is crucial for the operation of a thermoelectric device.[2, 30] Energy filtering is thought to be another mechanism of improving zT in nanocomposites where inclusions can separate higher energy electrons from lower energy electrons leading to increased Seebeck coefficients such as in Sb_2Te_3 composited with PEDOT.[31] In the $YB_{22}CN$ system, compositing with VB_2 is observed to increase the Seebeck coefficient by doping and electrical resistivity by creating a nanoweb of conductive pathways,[32] similar to what is described as the CAFE effect in $Yb_{14}MgSb_{11}$ – micron iron nano composite where the resistivity is decreased without changing the Seebeck coefficient.[33] Furthermore, an annealed nanograin model suggests that annealing defective nanoparticles creates a non-defective core with nanoparticle grain boundaries high in ionized impurities to achieve charge balance. This results in a nano particle with high Seebeck coefficient at the grain boundary and high electrical conductivity at the core leading to an overall increase in PF.[34]

Previously we have shown $Yb_{14}MgSb_{11}$ composited with micron-sized iron inclusions increased the elastic moduli and exhibited crack arresting leading to an improvement in material toughness over the pristine phase.[33] Additionally, it was shown that $Yb_{14}MgSb_{11}$ can be synthesized and composited through a quick mechanical ball milling followed by spark plasma sintering (SPS), which bypasses long annealing times traditionally required to synthesize $Yb_{14}MgSb_{11}$.[9, 24-25] An important finding was the chemically inert nature of the iron inclusions in the $Yb_{14}MgSb_{11}$ matrix.[33] Compositing with micron-sized iron inclusions leads to a 40% increase in PF for the $Yb_{14}MgSb_{11}$ composite with 8 Vol % iron and an 11% increase in zT for $Yb_{14}MgSb_{11}$

composite with 3 Vol % iron relative to $Yb_{14}MgSb_{11}$. In this work we improve on the $Yb_{14}MgSb_{11}$ iron composite by incorporating nano-scale iron into the bulk matrix *via* an *in situ* decomposition of $FeSb_2$. $FeSb_2$ is a stoichiometric orthorhombic phase that initially decomposes peritectically at 1018 K into ε-FeSb and an antimony rich liquid.[35-36] The phase diagram shows the complete melting at 1185 K into the liquidus.[37] At the temperatures of the chemical reaction to occur for $Yb_{14}MgSb_{11}$ (1473 K), $FeSb_2$ dissociates into Fe and Sb and the reaction shown below is expected to occur. Mg_3Sb_2 is used to suppress the vapor pressure of Mg.

$$14Yb + \frac{1}{3}Mg_3Sb_2 + \left(11 - 2x - \frac{2}{3}\right)Sb + xFeSb_2 = Yb_{14}MgSb_{11} + xFe \quad (5)$$

The *in situ* decomposition reaction of $FeSb_2$ (eq. 5) provides a clean, oxide-free, well dispersed iron as nano-inclusions (< 100 nm) in the bulk $Yb_{14}MgSb_{11}$ matrix.

Previously, the phonon lifetime (τ) of $Yb_{14}MnSb_{11}$ was determined from inelastic neutron scattering data to be $0.16 < \tau < 50$ ps,[38] from which the phonon mean free path (l) can be derived and found to be 0.30 nm to 94 nm. This result suggests that nanoscale inclusions of the order of 100 nm and less should scatter the long wavelength phonons in this system reducing κ_l.[39-40] Given that $Yb_{14}MSb_{11}$, M = Mg, Mn, are isostructural and the heat capacities of $Yb_{14}MnSb_{11}$ and $Yb_{14}MgSb_{11}$ are similar,[22, 33] the phonon mean free path should be roughly the same in both systems. We demonstrate that this nanoscale iron composite of $Yb_{14}MgSb_{11}$ exhibits further reduction in κ_l compared to the micron-sized iron composite[33] resulting in a 9% increase in *zT*.

2. Experimental

2.1 *Materials*: Materials were manipulated in an argon-filled glove box < 0.1 PPM of water and oxygen. Yb turnings of 200 mg ± 100 mg and Mg turnings of 100 mg ± 75 mg from ingots of Yb (Edge Tech, 99.95%) and Mg (99.9%, MagCan), respectively. Fe lump (Alfa Aesar 99.99%) and Sb shot (99.999%, 5N Plus) were used as received.

Mg_3Sb_2: Mg_3Sb_2 was synthesized as previously described in literature.[41]

$FeSb_2$: A 10g batch of Fe powder and Sb shot in a 1:2 molar ratio was milled for three hours with three ~10.75 g tungsten carbide balls in a 55 mL tungsten carbide vial set purchased from SPEX® SamplePrep in a SPEX 8000D mixer/ Mill. The material was scraped out and inserted into a 12.7 mm graphite die sealed with graphite foil. The material was hot pressed at 600 °C for

6 hours under active vacuum with 1 ton of pressure on the cross section. The resulting black ingot was milled in the vial set described above for 20 seconds with one 10.75 g tungsten carbide ball before use. The product was confirmed to be phase pure by Powder X-ray diffraction (PXRD) (see Supporting Information (SI), Figure S1).[42]

Caution: Finely divided metals are moisture and oxygen reactive and should be handled in an inert atmosphere.

2.2 *$Yb_{14}MgSb_{11}$ Composite*: Synthetic techniques were adapted from literature.[9] The elements and compounds were combined into a 10 g batch according to the molar amounts of 14.05 Yb, 0.4 Mg_3Sb_2, y $FeSb_2$, and 10.2-2y Sb. The value, y, is calculated from mass requirements to provide 1, 2, 3, 4, 6, and 7.3 Vol % iron, where 7.3 Vol % is the upper limit of iron incorporation based on the stoichiometry of $FeSb_2$ as an Sb source. The reagents were placed into a hermetically sealed tungsten carbide grinding vial set with one ~10.75 g tungsten carbide ball and milled for three hours. Excess Yb and Mg were employed to overcome experimentally observed losses and potential of surface oxide of each. After every hour of milling the material was scraped out of the vial and reinserted to ensure homogenization. The milled powder (3 g) was inserted into a graphite die with graphite spacers and reacted in a spark plasma sintering reactor (SPS, Thermal Technology LLC) under dynamic vacuum. Samples were heated to 1200 °C in 48 min and maintained at 1200 °C for 40 min. Pressure was increased from 10 MPa to 80 MPa over 10 min and retained during the reaction. Products were dark metallic pucks of ≥ 98% of theoretical density.

2.4 *Powder X-ray diffraction (PXRD)*: PXRD measurements were performed on a Bruker D8 Eco Advance diffractometer operating at 40 kV and 25 mA with Cu Kα radiation from 20° - 90° 2θ with a step size of 0.019°. Rietveld refinement was done with the software JANA2006.[43] The crystallographic information files for $Yb_{14}MgSb_{11}$, Yb_2O_3, $Yb_{11}Sb_{10}$, and Fe generated the Rietveld refinement models. First, a manual background and lattice parameters were fit, then a pseudo-Voigt function was used to generate the profile. The fits generated by Rietveld refinement, wRp, and GOF are provided in SI, Figure S2.

2.5 *Scanning electron microscopy (SEM):* SEM was performed using a Scios Dual beam SEM/FIB microscope. An Everhart-Thornley detector was used for secondary electron imaging. A window-less Oxford instruments X-max 50 furnished with a 50 mm^2 silicon drift detector was used for Energy dispersive X-ray spectroscopy (EDS). Sintered pellets mounted in epoxy were metallographically polished to a 0.1 μm finish for imaging.

2.7 *Magnetic characterizations*: Magnetic properties were studied at room temperature by magnetometry and the first-order reversal curve (FORC) method,[44-47] using a Princeton Measurements vibrating sample magnetometer (VSM) and a Quantum Design Magnetic Property Measurement System (MPMS3). The FORC distribution was calculated using the mixed second-order derivative of the magnetization (eq. 6),[44-46]

$$\rho\,(H, H_R) \equiv -\frac{1}{2M_S}\frac{\partial^2 M(H, H_R)}{\partial H\,\partial H_R} \quad (6),$$

where $M(H, H_R)$ is the magnetization measured at the applied field H with reversal field H_R, and M_S is the saturation magnetization. Coordinates were changed from (H, H_R) to (H_C, H_B) through the transformation defined by eq. 7:[46, 48-49]

$$H_B = \frac{1}{2}(H + H_R), H_C = \frac{1}{2}(H - H_R) \quad (7),$$

where H_B is the bias field and H_C is the local coercive field.

2.8 *Thermal conductivity*: Thermal diffusivity was measured with a Netzsch LFA 457 laser flash system. κ_{tot} is calculated from $D\ x\ C_P\ x\ \rho$ where D is diffusivity, ρ is temperature dependent density for $Yb_{14}MnSb_{11}$ and Fe scaled by weight percent, and C_P is heat capacity scaled by the rule of mixtures. The heat capacity approximation was shown to be a valid assumption in previously published $Yb_{14}MgSb_{11}$ iron composites.[33, 50-51] κ_l was calculated from the Wiedemann−Franz law (eq 8, 9).[8, 52] Experimental diffusivity data are provided in SI, Figure S3. Effective Medium Theory (EMT) calculations were employed using Maxwell-Euken (ME3) equation and the literature value for the temperature dependent thermal conductivity of iron. The size of iron particles was not considered.[53-54]

$$\left(\kappa_l = \kappa_{tot} - \kappa_e,\ \kappa_e = \frac{1}{\rho}LT\right) \quad (8), L = 1.5 + e^{\left(\frac{|S|}{116}\right)} \times\ 10^{-8}\ \frac{W}{K^2\Omega}) \quad (9)$$

2.9 *Resistivity Measurements*: Resistivity data were acquired under dynamic high vacuum using the Van der Pauw method. The experiment is described in detail in literature.[55] A sixth order polynomial was used to fit data for *zT* calculations. Heating and cooling data for experimental resistivity data are plotted in SI, Figure S3. Effective Medium Theory (EMT) calculations were performed using Maxwell-Euken (ME3) equation and the literature value for the temperature dependent resistivity of iron.[53-54]

2.10 *Seebeck measurements*: Seebeck coefficient measurements were done using a custom-built apparatus under high vacuum employing the light-pulse method, as previously described.[56] A sixth order polynomial was used to fit data for *zT* calculations. Heating and cooling data are plotted in SI, Figure S3.

3. Results and Discussion

3.1 *Compositional Characterization:* The *in situ* decomposition of $FeSb_2$ is used to supply antimony to form the $Yb_{14}MgSb_{11}$ phase as well as iron inclusions to the $Yb_{14}MgSb_{11}$ matrix. The well distributed $FeSb_2$ reagent and short reaction times of the SPS, as well as the *in situ* decomposition of the $FeSb_2$ into Fe domains intragranularly, leads to the resulting iron as nanoscale domains. The presence of nanoscale iron and the sample purity is confirmed by powder diffraction (Figure 1). The experimental patterns match the calculated patterns indicating phase purity. No evidence for $FeSb_2$ can be detected above the ~1 wt. % limit of PXRD but minor amounts of $Yb_{11}Sb_{10}$ (< 8 wt. %) and Yb_2O_3 (< 1.22 wt. %) impurities are observed for all samples. Previous work on $Yb_{14}MgSb_{11}$ showed that Yb_2O_3 is due to surface oxidation.[33] $Yb_{11}Sb_{10}$ is a common impurity in $Yb_{14}MSb_{11}$ systems (M = Mg, Mn) and has high thermal conductivity, low resistivity and low Seebeck coefficients.[57] While $Yb_{11}Sb_{10}$ is detrimental to the overall thermoelectric properties of $Yb_{14}MSb_{11}$, M = Mn, it has been shown that $Yb_{14}MnSb_{11}$ maintains thermoelectric performance with up to ~15% $Yb_{11}Sb_{10}$.[9] Since the $Yb_{11}Sb_{10}$ amounts are less than 8%, its presence is not considered to be detrimental to the thermoelectric properties. Results from Rietveld refinement are provided in Table 1. For iron amounts of 2 Vol % and higher, the amount of iron identified by Rietveld refinement is less than the nominal composition. This is attributed to some percentage of the iron being nanosized or amorphous and not contributing to the overall diffraction intensity. The amount of $Yb_{11}Sb_{10}$ also decreases after 2 Vol% Fe as observed in $Yb_{14}MgSb_{11}$ + micron-Fe composites where it was explained that Fe acts as a milling agent that allows Yb to be more evenly distributed, leading to less side phases.[33] The lattice parameters are all within experimental variations seen for $Yb_{14}MgSb_{11}$ implying slight differences in the defects of the samples; however, the heating and cooling thermoelectric data (provided in SI, Figure S3) show very little hysteresis indicating the defects, if present, are stable.[24-25, 33]

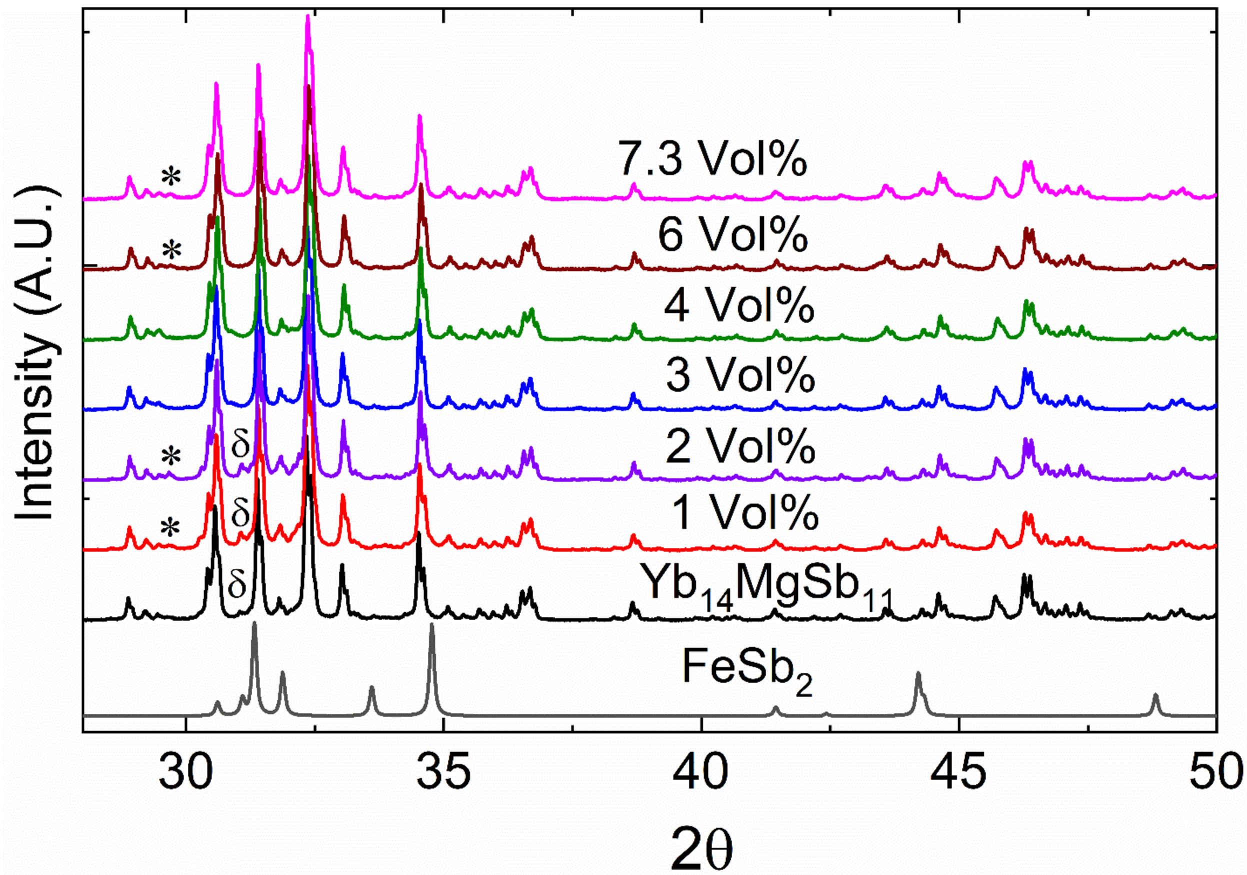

Figure 1. Observed PXRD patterns for $Yb_{14}MgSb_{11}$ + *x* volume % Fe (*x* Vol %) and the simulated pattern of $FeSb_2$. There is no evidence for $FeSb_2$ in the experimental data. Intensities for each pattern were normalized to 100% for the largest peak. * denotes Yb_2O_3 impurity and δ denotes $Yb_{11}Sb_{10}$ impurity.

Table 1. Lattice Parameters for $Yb_{14}MgSb_{11}$ and Rietveld Refinement Results‡ of $Yb_{14}MgSb_{11}$ + *x* Vol % Fe Composites

Sample	*a* (Å)	*c* (Å)	V (Å^3)	$Yb_{14}MgSb_{11}$ (Wt%)	$Yb_{11}Sb_{10}$ (Wt%)	Yb_2O_3 (Wt%)	Fe (Vol%)
$Yb_{14}MgSb_{11}$	16.604(4)	22.247(8)	6134.0(3)	94.78(12)	4.66(12)	0.56(4)	N/A
+1 Vol% Fe	16.602(5)	22.238(1)	6129.5(4)	90.7(2)	7.52(15)	0.74(5)	1.02(15)
+2 Vol% Fe	16.597(4)	22.234(1)	6125.2(3)	91.7(2)	6.40(14)	0.85(5)	0.97(15)
+3 Vol% Fe	16.604(4)	22.239(1)	6131.9(3)	96.74(19)	1.64(12)	0.29(5)	1.28(13)

+4 Vol% Fe	16.596(5)	22.231(1)	6123.0(3)	95.7(2)	1.93(14)	1.22(10)	1.65(15)
+6 Vol% Fe	16.595(5)	22.228(1)	6122.3(4)	96.7(3)	0	0.47(5)	2.7(2)
+7.3 Vol% Fe	16.601(4)	22.24(1)	6128.2(4)	94.12(19)	0.87(11)	0.90(5)	3.97(14)

‡wRp and GOF are provided in SI, Figure S2.

The morphology and size of iron inclusions were further probed by SEM and described below. Z-contrasted backscattered electron (BSE) images are shown in Figure 2A for 1, 4, and 7.3 Vol % iron composites. As iron concentration increases the black inclusions observed in the images corresponding to iron increase. Agglomerations of iron are scattered but present; however, the dominant features are small circular iron inclusions. This differs from previously reported $Yb_{14}MgSb_{11}$ iron composites synthesized from micron-iron which showed elongated iron inclusions (6 Vol % composites prepared from micron-iron and $FeSb_2$ are shown for comparison in SI, Figure S4).[33] Circular inclusions have been shown to lead to a lower κ_l compared to long inclusions in polymers.[27] Neither the morphology nor the size of the iron inclusions change after three annealing cycles to 1273 K (Figure 2) or after a 168 hour dwell at 1273 K (SI, Figure S5) indicating that once the $Yb_{14}MgSb_{11}$ matrix is formed the iron particles do not diffuse. Figure 2B shows EDS line scans. Multiple iron particles in the 100 nm size range (nanodomain) are present in all samples (SI, Figure S6) and are sustained after cycling to 1273 K. Topological and BSE images at multiple magnifications for 1, 2, 3, 4, 6, 7.3 Vol % iron composites are provided in SI, Figure S6.

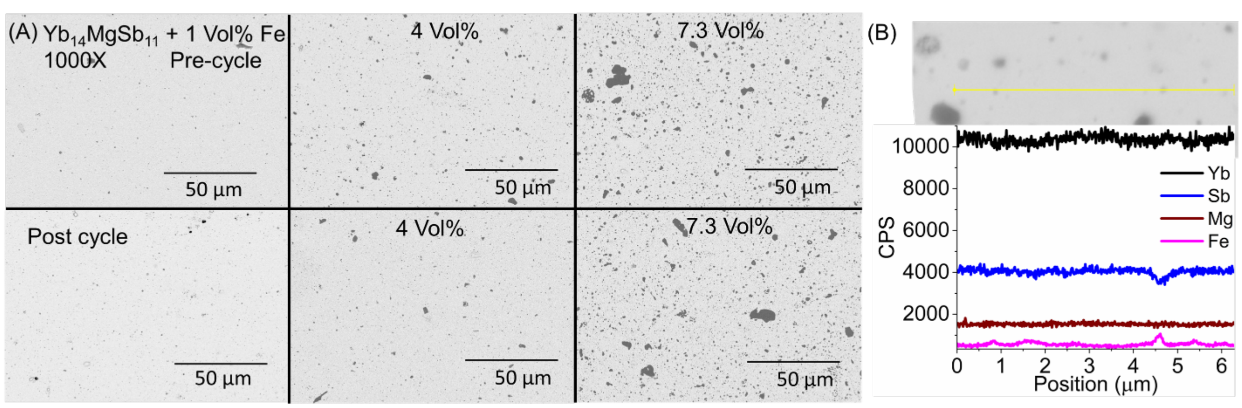

Figure 2. (A) BSE images (Z contrast) of $Yb_{14}MgSb_{11}$ + 1, 4, 7.3 Vol % iron composites before (top) and after cycling to 1273 K (bottom). (B) Line scan of $Yb_{14}MgSb_{11}$ + 7.3 Vol % iron showing that the black spots are iron and some are about 100 nm.

3.2 *Magnetic Characteristics:* To study the interactions between the Fe inclusions within the samples, we have analyzed the FORC distribution in the (H_C, H_B) coordinates. In the prior study of $Yb_{14}MgSb_{11}$ with micron-iron composites, the FORC distribution exhibited two primary features, a vertical ridge along the H_B axis and a horizontal tail along the H_C axis near $H_B = 0$ (SI, Figure S7).[33] In the present study, the FORC distributions for $Yb_{14}MgSb_{11}$ + 1, 3, and 6 Vol % Fe composites made from $FeSb_2$ exhibit seemingly similar features, as shown in Figure 3A. However, close examination reveals certain qualitative distinctions. In particular, the 1 Vol % Fe sample shows a prominent horizontal FORC ridge at $H_B = 0$ along the H_C axis, and a small spread along H_B at lower switching fields (H_C). The striking horizontal ridge, extending to H_C > 4 kOe, is characteristic of a collection of non-interacting single domain particles[49, 58-59] where the coercivity is enhanced due to the ultrasmall size of the magnetic inclusions.[47] This indicates that most of the iron inclusions are not interacting; the very limited spread along H_B suggests that some residual interactions between iron inclusions exist, but they are at a much weaker level compared to samples with higher iron contents. This is consistent with the smaller size and homogenous distribution of the iron clusters seen in the SEM images for the 1 Vol % sample (Figure 2, and SI, Figure S6). As the iron content increases, the horizontal FORC feature along the H_C axis diminishes quickly and the vertical FORC ridge along the H_B axis becomes more pronounced (Figure 3A). This indicates the presence of a significant demagnetizing dipolar interaction[60-61] between the clusters when there are more, larger iron inclusions in the 3 and 6 Vol % samples. Furthermore, by integrating the FORC distribution along the H_C axis, its projection onto the H_B axis is obtained, as shown in Figure 3B. This bias field distribution is a manifestation of how strongly the neighboring magnetic entities interact with one another magnetically. In the 1 Vol % sample, given its small iron cluster size and low iron content, a sharp peak centered at H_B = 0 with a very narrow width and a flat background is observed. Thus, most of the iron clusters switch independently from other clusters. As the iron cluster breaks down in size from micron-scale to nanoscale ($FeSb_2$), the average distance between adjacent clusters also decreases. For a certain iron content, the ratio between interparticle distance and particle average diameter decreases, leading to stronger dipolar interactions. The coercivity of the iron clusters also varies with the particle size, which is manifested in the switching field distribution (horizontal tail) in the FORC diagrams. The more pronounced horizontal FORC features in the $FeSb_2$ samples, together with their longer spread along the H_C axis, indicate overall higher coercivities and a larger coercivity distribution. It is well-known that as magnetic particle size decreases, the coercivity first increases to a maximum and eventually decreases due to thermal fluctuations.[47, 62] For 3 and 6 Vol % samples, the FORC projection along H_B gets broader and appreciable FORC distribution extends beyond H_B > 4kOe, indicating a strong dipolar interaction among iron clusters. As iron clusters size decreases from micron-iron (a few microns) to nanoscale iron (a few hundreds of nm), their coercivity would increase, which is indeed captured by the FORC distributions.

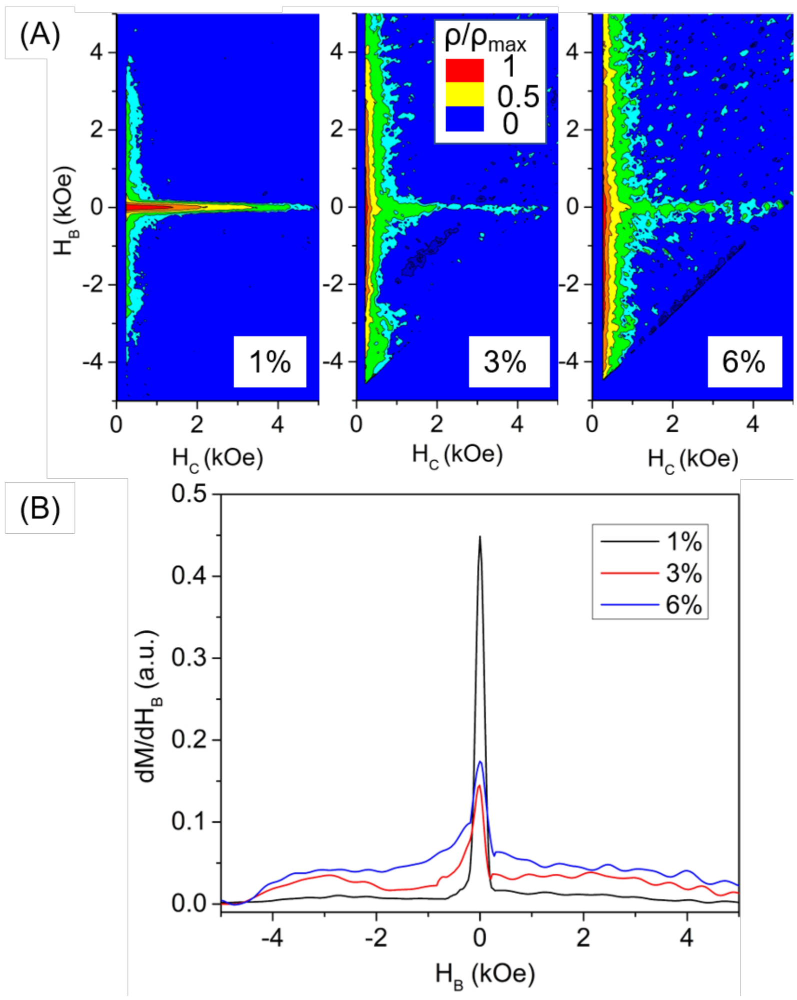

Figure 3. (A) FORC distributions for $Yb_{14}MgSb_{11}$ + 1, 3, 6 Vol % iron prepared from $FeSb_2$. (B) Corresponding bias field distribution extracted by the projection of the FORC distribution in (A) onto the H_B axis.

3.3 *Electronic Transport*: A material with tunable electronic properties provides added flexibility for the design of thermoelectric couples and generators and composites can provide an important avenue for optimization.[63] Figure 4A shows resistivity vs temperature data for

$Yb_{14}MgSb_{11}$ composites along with their respective Effective Medium Theory (EMT) calculated resistivities. All samples exhibit the semi-metallic temperature dependent behavior that decreases with Fe concentration, consistent with behavior observed in the $Yb_{14}MgSb_{11}$ micron-iron composites in which the reduction of resistivity was attributed to composite assisted funneling of electrons (CAFE) where similar to the 'conductive nano-network' in $YB_{22}CN$ system, charge carriers are funneled through the conductive inclusions reducing electrical resistivity overall.[32-33, 64] The resistivity calculated by EMT is much higher than the measured values. This was also observed in tungsten composited $Yb_{14}MnSb_{11}$,[65] $LaTe_{1.46}$ composited with Ni,[66] and $Yb_{14}MgSb_{11}$ composited with micron-iron[33] suggesting that a weighted average of the metallic inclusion and bulk matrix does not account for the full reduction in resistivity. In composites with metallic inclusions, the inclusions act as voids that do not contribute significantly to the Seebeck coefficient,[66-67] so any change in Seebeck coefficient is attributed to a change in defect concentration. The consistent Seebeck values shown in Figure 4B (within ~7% error, 231 ± 16 μV/K), observed for all iron concentrations, thus confirm that no changes to carrier concentration have occurred. This suggests the reduction of resistivity when compared to the EMT derived values cannot be explained by changes to carrier concentration (i.e. no additional defects form with the addition of iron). Efforts to probe the carrier concentration of the system by temperature dependent Hall effect data were undertaken but did not provide fruitful results, as irons anomalous hall effect drowned out the signal from the $Yb_{14}MgSb_{11}$ as discussed in the work done on the $Yb_{14}MgSb_{11}$ – micron Fe composite.[33, 68]

Figure 4B demonstrates that the temperature dependent Seebeck coefficient is the same for all samples, thus any increases in *PF* (Figure 4C), particularly apparent at higher temperatures, originate from decreases in resistivity. This increase in *PF* demonstrates that the electronic properties can be tuned without changes to the carrier concentration. When combined with traditional doping optimization, this approach can be used to further maximize *zT* or can be used to maximize device ZT.[69-70]

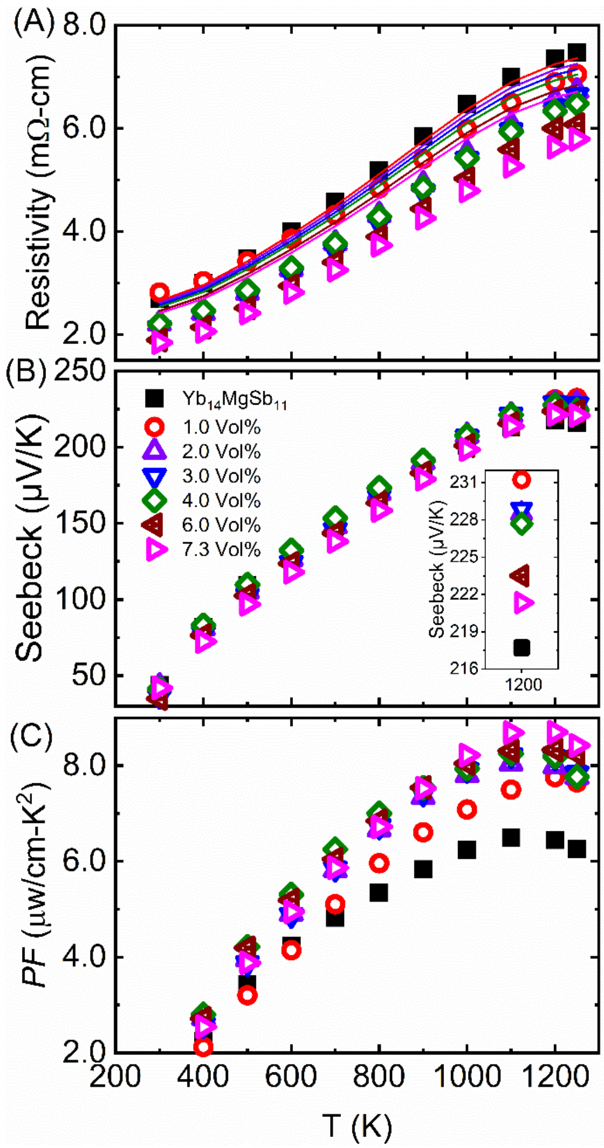

Figure 4: (A) Resistivity vs temperature for $Yb_{14}MgSb_{11}$ composited with x Vol % iron and resistivity predicted by Effective Medium Theory (EMT). Solid lines of corresponding color represent resistivity predicted by EMT. (B) Seebeck vs temperature for $Yb_{14}MgSb_{11}$ + x Vol % iron. The inlay shows the value of Seebeck coefficient at peak performance (1200 K). (C) Power Factor vs temperature for $Yb_{14}MgSb_{11}$ + x Vol % iron. The largest increase in *PF* is observed in the 7.3 Vol % composite consistent with the sample exhibiting the lowest resistivity.

3.4 *Thermal Conductivity*: The temperature dependent κ_{tot}, modeled EMT κ_{tot}, and κ_l calculated from Eq. 8 are shown in Figure 5. The κ_{tot} remains constant (>900 K) as the concentration of iron increases, that is until the iron concentration is above 4 Vol %. In contrast, 1 - 6 Vol % samples have almost identical κ_l (>900 K) which suggests the iron inclusions are small enough to interfere with the longer wavelength phonons further supporting the notion that a sufficient number of Fe inclusions are < 100 nm.[67] This result is consistent with the PXRD, SEM, and FORC which indicate that at least some of the iron is in the nanodomain. Another indicator of long wavelength phonon interference is the nearly temperature independent κ_l behavior especially at higher temperatures of the nano-iron composite samples—a behavior not observed in the micro iron composites[33] (Figure 5B, 6 Vol % micron-iron composite). At low temperature the 1 Vol% sample has a larger κ_l than the $Yb_{14}MgSb_{11}$ sample which could be due to a larger $Yb_{11}Sb_{10}$ concentration which is metallic. We do note that the data follow the thermal conductivity trends predicted by EMT better than other $Yb_{14}\mathit{M}Sb_{11}$ composites (*M* = Mg, Mn),[33, 65] perhaps because the nano-composites do not experience the effects of percolation.[67] Overall, the 6 Vol % iron sample has a κ_l that is 12 % lower than the 6 Vol % sample made from micron-iron, suggesting that additional scattering mechanisms are introduced when nano inclusions are present. This conclusion of course assumes that the Wiedemann-Franz law accurately predicts κ_e for composite materials.

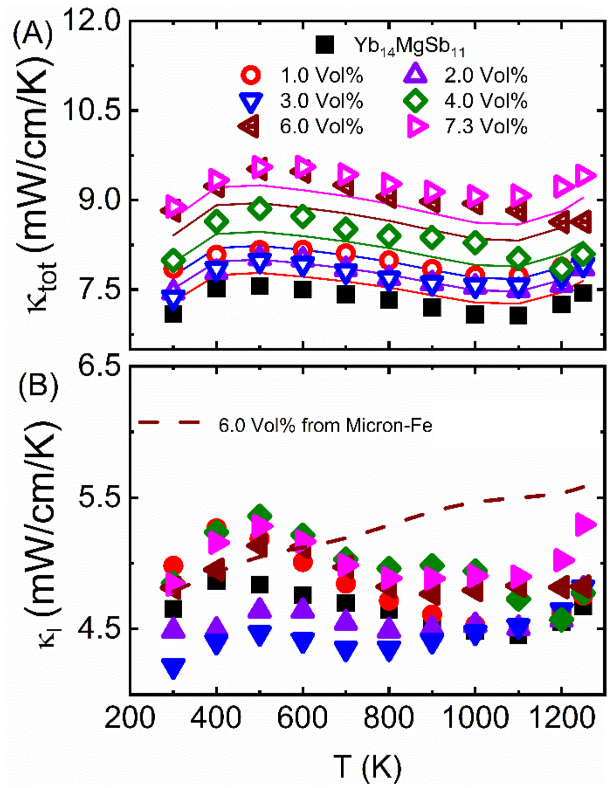

Figure 5: (A) Thermal conductivity vs temperature for $Yb_{14}MgSb_{11}$ + *x* Vol % iron. Solid lines of corresponding color represent κ_{tot} predicted by EMT. (B) Lattice thermal conductivity vs temperature for all samples. Dashed line represents κ_l for 6 Vol % micron-sized iron composite.[33] The 6 Vol % nano-iron composite exhibits considerably lower lattice thermal conductivity relative to micron-iron composite, particularly at higher temperatures.

3.8 *Figure of Merit, zT*: The peak *zT* (Figure 6) at 1, 2, 3 Vol % iron composites is 1.25 at 1200 K with 4, 6 Vol % very close at 1.20 which is on par with the best reported *zT* for $Yb_{14}MgSb_{11}$ (1.2),[25] and is a 20% improvement when compared to $Yb_{14}MgSb_{11}$ prepared for this study. This is a modest improvement over the peak *zT* of the $Yb_{14}MgSb_{11}$ micron-iron composites which topped out at a *zT* of 1.18. Samples made from micron-iron begin to decrease in *zT* after 4 Vol % iron and at 8 Vol % iron are down to a *zT* of 1.02 at 1200 K. In contrast, the 7.3 volume % iron sample made from $FeSb_2$ remains at a *zT* of 1.1 at 1200 K. The temperature averaged figure of merit, ZT, for the 3 Vol % iron sample is 1.12 which is higher than both $Yb_{14}MnSb_{11}$ and $Yb_{14}MgSb_{11}$ (1.10, 1.07, respectively) indicating slightly better overall performance due to a reduction of thermal conductivity resulting from the presence of nano iron. The mechanical robustness of the material improves as a function of iron concentration so having a composite that retains thermoelectric performance at high iron concentrations is critical for large scale manufacturing.[33]

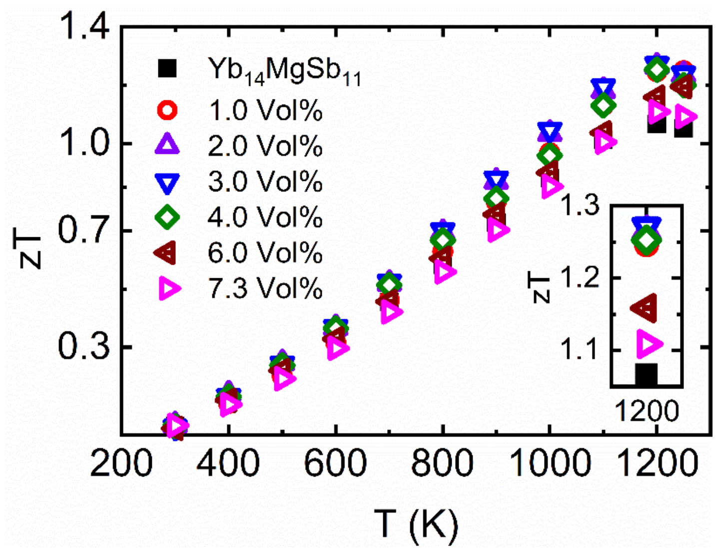

Figure 6. *zT vs* temperature for $Yb_{14}MgSb_{11}$ + *x* Vol % iron.

4. Summary:

In this work we have employed a novel *in situ* method of delivering well dispersed nanosized iron via rapid high temperature decomposition of $FeSb_2$ and concomitant formation of $Yb_{14}MgSb_{11}$ with well dispersed nanoscale iron inclusions. SEM, PXRD, and FORC show the $Yb_{14}MgSb_{11}$ matrix contains nanosized iron particles that are well dispersed compared to $Yb_{14}MgSb_{11}$ composited from micron-iron powder.[33] FORC diagrams reveal mostly non-interacting iron inclusions with significantly enhanced coercivities for the 1 Vol % sample, and strongly dipolar interacting iron inclusions for the 3 and 6 Vol % samples. The changes of the magnetic properties are much more drastic compared to the micron-iron composites previously reported,[33] as the average iron particle size are reduced to the nanoscale. The morphology of the iron is preserved after cycling to 1273 K three times for all samples and annealing at 1273 K for 168 hours for the 3 Vol % sample. The resistivity decreases rapidly as a function of iron without significantly affecting the Seebeck coefficient. These results provide a 43% Power Factor (*PF)* improvement at 7.3 Vol % iron compared to $Yb_{14}MgSb_{11}$. When combined with traditional doping optimization, this approach can be used to further maximize zT or can be used to maximize device ZT. The smaller circular iron inclusions provide a decrease in κ_l in all samples. The decreased κ_{tot} and PF improvement lead to a 9 % improvement in zT at 1, 2, 3 Vol % compared to samples synthesized with micron-iron and maintain their zT up to 7.3 Vol % iron allowing for more iron incorporation. Additionally, the 3 Vol % iron sample has a higher integrated *ZT* than both $Yb_{14}MnSb_{11}$ and $Yb_{14}MgSb_{11}$.

5. Supporting Information

The Supporting Information is available free of charge on the ACS Publications website at DOI:

PXRD of $FeSb_2$ compared with the calculated diffraction pattern, plots of Rietveld refinements of all phases investigated in this study, heating and cooling resistivity, Seebeck, and diffusivity data, comparison SEM Z-contrast for $Yb_{14}MgSb_{11}$ + 6 Vol % iron composites prepared from $FeSb_2$ versus micron-sized Fe, SEM BSE image of $Yb_{14}MgSb_{11}$ + 6 Vol % iron composite from $FeSb_2$ after annealing at 1273 K for 168 h, topological and Z-contrasted SEM images at 500X, 1000X, 2500X, and 50000X for all composite samples studied, and FORC distributions for samples prepared from $FeSb_2$ and micron-sized iron.

6. Author Information:

Corresponding Authors* Email: sabah.k.bux@jpl.nasa.gov, smkauzlarich@ucdavis.edu

ORCID: Christopher J. Perez: 0000-0002-1088-0190, Zhijie Chen: 0000-0002-3594-5560, Willie B. Beeson: 0000-0002-5207-7590, Sevan Chanakian: 0000-0003-0482-4069: Sabah K. Bux: 0000-0002-5372-354X, Kai Liu: 0000-0001-9413-6782, Susan M. Kauzlarich: 0000-0002-3627-237X.

7. Notes:

The authors declare no competing financial interest.

8. Acknowledgments: The authors thank George Nakatsukasa and Gregory Gerig for assistance with thermal diffusivity and Seebeck measurements, respectively. S.C.'s contributions are based upon work supported by the National Science Foundation Graduate Research Fellowship Program award number DGE-1848739. This work was supported by NEUP, NSF DMR-1709382, DMR-2001156 and the National Aeronautics and Space Administration (NASA) Science Missions Directorate's Radioisotope Power Systems Program. Work at GU was supported by the NSF (ECCS-1933527). The acquisition of a Magnetic Property Measurements System (MPMS3) at GU, which was used in this investigation was supported by the NSF (DMR-1828420). Part of this work was conducted at the Jet Propulsion Laboratory California Institute of Technology under contract with NASA and funding from the Science Mission Directorate's Radioisotope Power Systems program.

9. References:

1. Liebl, J.; Neugebauer, S.; Eder, A.; Linde, M.; Mazar, B.; Stütz, W., The thermoelectric generator from BMW is making use of waste heat. *MTZ worldwide* **2009,** *70*, 4-11.
2. Fleurial, J. P., Thermoelectric Power Generation Materials: Technology and Application Opportunities. *JOM* **2009,** *61* (4), 79-85.
3. Kraemer, D.; Poudel, B.; Feng, H. P.; Caylor, J. C.; Yu, B.; Yan, X.; Ma, Y.; Wang, X.; Wang, D.; Muto, A.; McEnaney, K.; Chiesa, M.; Ren, Z.; Chen, G., High-performance flat-panel solar thermoelectric generators with high thermal concentration. *Nat Mater* **2011,** *10* (7), 532-8.
4. Akinaga, H., Recent advances and future prospects in energy harvesting technologies. *Jpn. J. Appl. Phys.* **2020,** *59* (11), 110201.
5. Petsagkourakis, I.; Tybrandt, K.; Crispin, X.; Ohkubo, I.; Satoh, N.; Mori, T., Thermoelectric materials and applications for energy harvesting power generation. *Science and Technology of Advanced Materials* **2018,** *19* (1), 836-862.
6. Kanoun, O.; Bradai, S.; Khriji, S.; Bouattour, G.; El Houssaini, D.; Ben Ammar, M.; Naifar, S.; Bouhamed, A.; Derbel, F.; Viehweger, C., Energy-Aware System Design for Autonomous Wireless Sensor Nodes: A Comprehensive Review. *Sensors* **2021,** *21* (2), 548.
7. Ouerdane, H.; Apertet, Y.; Goupil, C.; Lecoeur, P., Continuity and boundary conditions in thermodynamics: From Carnot's efficiency to efficiencies at maximum power. *The European Physical Journal Special Topics* **2015,** *224* (5), 839-864.
8. Snyder, G. J.; Toberer, E. S., Complex thermoelectric materials. *Nat. Mater.* **2008,** *7* (2), 105-114.
9. Grebenkemper, J. H.; Hu, Y. F.; Barrett, D.; Gogna, P.; Huang, C. K.; Bux, S. K.; Kauzlarich, S. M., High Temperature Thermoelectric Properties of $Yb_{14}MnSb_{11}$ Prepared from Reaction of MnSb with the Elements. *Chem. Mater.* **2015,** *27* (16), 5791-5798.

10. Zeier, W. G.; Zevalkink, A.; Gibbs, Z. M.; Hautier, G.; Kanatzidis, M. G.; Snyder, G. J., Thinking Like a Chemist: Intuition in Thermoelectric Materials. *Angewandte Chemie* **2016,** *55* (24), 6826-41.
11. Zebarjadi, M.; Joshi, G.; Zhu, G.; Yu, B.; Minnich, A.; Lan, Y.; Wang, X.; Dresselhaus, M.; Ren, Z.; Chen, G., Power factor enhancement by modulation doping in bulk nanocomposites. *Nano Lett.* **2011,** *11* (6), 2225-30.
12. Liu, W. S.; Yan, X.; Chen, G.; Ren, Z. F., Recent advances in thermoelectric nanocomposites. *Nano Energy* **2012,** *1* (1), 42-56.
13. Lory, P. F.; Pailhes, S.; Giordano, V. M.; Euchner, H.; Nguyen, H. D.; Ramlau, R.; Borrmann, H.; Schmidt, M.; Baitinger, M.; Ikeda, M.; Tomes, P.; Mihalkovic, M.; Allio, C.; Johnson, M. R.; Schober, H.; Sidis, Y.; Bourdarot, F.; Regnault, L. P.; Ollivier, J.; Paschen, S.; Grin, Y.; de Boissieu, M., Direct measurement of individual phonon lifetimes in the clathrate compound Ba7.81Ge40.67Au5.33. *Nat Commun* **2017,** *8* (1), 491.
14. Toberer, E. S.; Cox, C. A.; Brown, S. R.; Ikeda, T.; May, A. F.; Kauzlarich, S. M.; Snyder, G. J., Traversing the Metal-Insulator Transition in a Zintl Phase: Rational Enhancement of Thermoelectric Efficiency in $Yb_{14}Mn_{1-x}Al_xSb_{11}$. *Adv. Funct. Mater.* **2008,** *18* (18), 2795-2800.
15. Toberer, E. S.; Brown, S. R.; Ikeda, T.; Kauzlarich, S. M.; Snyder, G. J., High thermoelectric efficiency in lanthanum doped $Yb_{14}MnSb_{11}$. *Appl Phys Lett* **2008,** *93* (6), 062110.
16. Hu, Y. F.; Bux, S. K.; Grebenkemper, J. H.; Kauzlarich, S. M., The effect of light rare earth element substitution in $Yb_{14}MnSb_{11}$ on thermoelectric properties. *Journal of Materials Chemistry C* **2015,** *3* (40), 10566-10573.
17. Grebenkemper, J. H.; Klemenz, S.; Albert, B.; Bux, S. K.; Kauzlarich, S. M., Effects of Sc and Y substitution on the structure and thermoelectric properties of $Yb_{14}MnSb_{11}$. *J. Solid State Chem.* **2016,** *242*, 55-61.
18. Cox, C. A.; Brown, S. R.; Snyder, G. J.; Kauzlarich, S. M., Effect of Ca Doping on the Thermoelectric Performance of Yb14MnSb11. *J. Electron. Mater.* **2010,** *39* (9), 1373-1375.
19. Yi, T.; Abdusalyamova, M. N.; Makhmudov, F.; Kauzlarich, S. M., Magnetic and transport properties of Te doped $Yb_{14}MnSb_{11}$. *Journal of Materials Chemistry* **2012,** *22* (29), 14378-14384.
20. Brown, S. R.; Toberer, E. S.; Ikeda, T.; Cox, C. A.; Gascoin, F.; Kauzlarich, S. M.; Snyder, G. J., Improved Thermoelectric Performance in $Yb_{14}Mn_{1-x}Zn_xSb_{11}$by the Reduction of Spin-Disorder Scattering. *Chem. Mater.* **2008,** *20* (10), 3412-3419.
21. Hu, Y.; Cerretti, G.; Kunz Wille, E. L.; Bux, S. K.; Kauzlarich, S. M., The remarkable crystal chemistry of the $Ca_{14}AlSb_{11}$ structure type, magnetic and thermoelectric properties. *Journal of Solid State Chemistry* **2019,** *271*, 88-102.
22. Hu, Y. F.; Wang, J.; Kawamura, A.; Kovnir, K.; Kauzlarich, S. M., $Yb_{14}MgSb_{11}$ and $Ca_{14}MgSb_{11}$-New Mg-Containing Zintl Compounds and Their Structures, Bonding, and Thermoelectric Properties. *Chemistry of Materials* **2015,** *27* (1), 343-351.
23. Hu, Y. F.; Lee, K.; Kauzlarich, S. M., Optimization of $Ca_{14}MgSb_{11}$ through Chemical Substitutions on Sb Sites: Optimizing Seebeck Coefficient and Resistivity Simultaneously. *Crystals* **2018,** *8* (5).
24. Hu, Y.; Wang, J.; Kawamura, A.; Kovnir, K.; Kauzlarich, S. M., $Yb_{14}MgSb_{11}$ and $Ca_{14}MgSb_{11}$—New Mg-Containing Zintl Compounds and Their Structures, Bonding, and Thermoelectric Properties. *Chem. Mater.* **2014,** *27* (1), 343-351.
25. Justl, A. P.; Cerretti, G.; Bux, S. K.; Kauzlarich, S. M., Hydride assisted synthesis of the high temperature thermoelectric phase: $Yb_{14}MgSb_{11}$. *J. Appl. Phys.* **2019,** *126* (16), 165106.
26. Uvarov, C. A.; Ortega-Alvarez, F.; Kauzlarich, S. M., Enhanced High-Temperature Thermoelectric Performance of $Yb_{14-x}Ca_xMnSb_{11}$. *Inorganic Chemistry* **2012,** *51* (14), 7617-7624.
27. Burger, N.; Laachachi, A.; Ferriol, M.; Lutz, M.; Toniazzo, V.; Ruch, D., Review of thermal conductivity in composites: Mechanisms, parameters and theory. *Prog. Polym. Sci.* **2016,** *61*, 1-28.
28. Liu, Z.; Mao, J.; Liu, T.-H.; Chen, G.; Ren, Z., Nano-microstructural control of phonon engineering for thermoelectric energy harvesting. *MRS Bull.* **2018,** *43* (3), 181-186.

29. Liu, Y.; Zhang, Y.; Ortega, S.; Ibanez, M.; Lim, K. H.; Grau-Carbonell, A.; Marti-Sanchez, S.; Ng, K. M.; Arbiol, J.; Kovalenko, M. V.; Cadavid, D.; Cabot, A., Crystallographically Textured Nanomaterials Produced from the Liquid Phase Sintering of $Bi_xSb_{2-x}Te_3$ Nanocrystal Building Blocks. *Nano Lett.* **2018,** *18* (4), 2557-2563.
30. Rogl, G.; Rogl, P., How nanoparticles can change the figure of merit, ZT, and mechanical properties of skutterudites. *Materials Today Physics* **2017,** *3*, 48-69.
31. Nandihalli, N.; Liu, C.-J.; Mori, T., Polymer based thermoelectric nanocomposite materials and devices: Fabrication and characteristics. *Nano Energy* **2020,** *78*, 105186.
32. Mori, T.; Hara, T., Hybrid effect to possibly overcome the trade-off between Seebeck coefficient and electrical conductivity. *Scripta Mater.* **2016,** *111*, 44-48.
33. Perez, C. J.; Qi, X.; Chen, Z. J.; Bux, S. K.; Chanakain, S.; Li, B.; Liu, K.; Dhall, R.; Bustillo, K. C.; Kauzlarich, S. M., Improved Power Factor and Mechanical Properties of Composites of $Yb_{14}MgSb_{11}$ with Iron. *Acs Appl Energ Mater* **2020,** *3* (3), 2147-2159.
34. Zianni, X., The annealed-nanograin phase: A route to simultaneous increase of the conductivity and the Seebeck coefficient and high thermoelectric performance. *J. Appl. Phys.* **2019,** *126* (19), 194301.
35. Petrovic, C.; Kim, J. W.; Bud'ko, S. L.; Goldman, A. I.; Canfield, P. C.; Choe, W.; Miller, G. J., Anisotropy and large magnetoresistance in the narrow-gap semiconductor $FeSb_2$. *Physical Review B* **2003,** *67* (15), 155205.
36. Boa, D.; Hassam, S.; Rogez, J.; Kotchi, K. P., The iron–antimony system: enthalpies of formation of the $FeSb_2$ and ε-FeSb phases. *Journal of Alloys and Compounds* **2004,** *365* (1-2), 228-232.
37. Massalski, T. B.; Subramanian, P. R.; Okamoto, H.; Kacprzak , L., *Binary alloy phase diagrams*. 2nd ed.; ASM International: Materials Park, Ohio, 1990.
38. Möchel, A.; Sergueev, I.; Wille, H. C.; Juranyi, F.; Schober, H.; Schweika, W.; Brown, S. R.; Kauzlarich, S. M.; Hermann, R. P., Lattice dynamics in the thermoelectric Zintl compound $Yb_{14}MnSb_{11}$. *Phys. Rev. B* **2011,** *84* (18), 184303.
39. He, J.; Kanatzidis, M. G.; Dravid, V. P., High performance bulk thermoelectrics via a panoscopic approach. *Mater. Today* **2013,** *16* (5), 166-176.
40. Zhao, L. D.; Dravid, V. P.; Kanatzidis, M. G., The panoscopic approach to high performance thermoelectrics. *Energy Environ. Sci.* **2014,** *7* (1), 251-268.
41. Ohno, S.; Imasato, K.; Anand, S.; Tamaki, H.; Kang, S. D.; Gorai, P.; Sato, H. K.; Toberer, E. S.; Kanno, T.; Snyder, G. J., Phase Boundary Mapping to Obtain n-type Mg_3Sb_2-Based Thermoelectrics. *Joule* **2018,** *2* (1), 141-154.
42. Holseth, H.; Kjekshus, A., Compounds with the marcasite type crystal structure pt. 4. Crystal structure of $FeSb_2$. *Acta Chem. Scand.* **1969,** *23* (9), 3043-3050.
43. Petříček, V.; Dušek, M.; Palatinus, L., Crystallographic Computing System JANA2006: General features. In *Zeitschrift für Kristallographie - Crystalline Materials*, 2014; Vol. 229, p 345.
44. Pike, C. R.; Roberts, A. P.; Verosub, K. L., Characterizing interactions in fine magnetic particle systems using first order reversal curves. *J. Appl. Phys.* **1999,** *85* (9), 6660-6667.
45. Davies, J. E.; Hellwig, O.; Fullerton, E. E.; Denbeaux, G.; Kortright, J. B.; Liu, K., Magnetization reversal of Co/Pt multilayers: Microscopic origin of high-field magnetic irreversibility. *Phys. Rev. B* **2004,** *70* (22), 224434.
46. Gilbert, D. A.; Zimanyi, G. T.; Dumas, R. K.; Winklhofer, M.; Gomez, A.; Eibagi, N.; Vicent, J. L.; Liu, K., Quantitative Decoding of Interactions in Tunable Nanomagnet Arrays Using First Order Reversal Curves. *Sci. Rep.* **2014,** *4*, 4204.
47. Rahman, M. T.; Dumas, R. K.; Eibagi, N.; Shams, N. N.; Wu, Y.-C.; Liu, K.; Lai, C.-H., Controlling magnetization reversal in Co/Pt nanostructures with perpendicular anisotropy. *Appl. Phys. Lett.* **2009,** *94* (4), 042507.
48. Cho, S. J.; Shahin, A. M.; Long, G. J.; Davies, J. E.; Liu, K.; Grandjean, F.; Kauzlarich, S. M., Magnetic and Mossbauer spectral study of core/shell structured Fe/Au nanoparticles. *Chem. Mater.* **2006,** *18* (4), 960-967.

49. De Toro, J. A.; Vasilakaki, M.; Lee, S. S.; Andersson, M. S.; Normile, P. S.; Yaacoub, N.; Murray, P.; Sánchez, E. H.; Muñiz, P.; Peddis, D.; Mathieu, R.; Liu, K.; Geshev, J.; Trohidou, K. N.; Nogués, J., Remanence Plots as a Probe of Spin Disorder in Magnetic Nanoparticles. *Chem. Mater.* **2017,** *29* (19), 8258-8268.
50. Ravi, V.; Firdosy, S.; Caillat, T.; Brandon, E.; Van der Walde, K.; Maricic, L.; Sayir, A., Thermal Expansion Studies of Selected High-Temperature Thermoelectric Materials. *J. Electron. Mater.* **2009,** *38* (7), 1433-1442.
51. Cleaves, H. E.; Hiegel, J. M., Properties of high-purity iron. *Journal of Research of the National Bureau of Standards* **1942,** *28* (5), 643-667.
52. Kim, H. S.; Gibbs, Z. M.; Tang, Y. L.; Wang, H.; Snyder, G. J., Characterization of Lorenz number with Seebeck coefficient measurement. *APL Mater.* **2015,** *3* (4), 041506.
53. Gong, L. L.; Wang, Y. H.; Cheng, X. D.; Zhang, R. F.; Zhang, H. P., A novel effective medium theory for modelling the thermal conductivity of porous materials. *Int. J. Heat Mass Transfer* **2014,** *68*, 295-298.
54. Fulkerson, W.; Moore, J. P.; McElroy, D. L., Comparison of the Thermal Conductivity, Electrical Resistivity, and Seebeck Coefficient of a High - Purity Iron and an Armco Iron to 1000°C. *Journal of Applied Physics* **1966,** *37* (7), 2639-2653.
55. Borup, K. A.; Toberer, E. S.; Zoltan, L. D.; Nakatsukasa, G.; Errico, M.; Fleurial, J. P.; Iversen, B. B.; Snyder, G. J., Measurement of the electrical resistivity and Hall coefficient at high temperatures. *Rev. Sci. Instrum.* **2012,** *83* (12), 123902-123909.
56. Wood, C.; Zoltan, D.; Stapfer, G., Measurement of Seebeck Coefficient Using a Light-Pulse. *Rev. Sci. Instrum.* **1985,** *56* (5), 719-722.
57. Brown, S. R.; Kauzlarich, S. M.; Gascoin, F.; Jeffrey Snyder, G., High-temperature thermoelectric studies of $A_{11}Sb_{10}$ (A=Yb, Ca). *J. Solid State Chem.* **2007,** *180* (4), 1414-1420.
58. Dumas, R. K.; Li, C. P.; Roshchin, I. V.; Schuller, I. K.; Liu, K., Magnetic fingerprints of sub-100 nm Fe dots. *Phys. Rev. B* **2007,** *75* (13), 134405.
59. Davies, J. E.; Wu, J.; Leighton, C.; Liu, K., Magnetization Reversal and Nanoscopic Magnetic Phase Separation in $La_{1-x}Sr_xCoO_3$. *Phys. Rev. B* **2005,** *72*, 134419.
60. Kou, X.; Fan, X.; Dumas, R. K.; Lu, Q.; Zhang, Y.; Zhu, H.; Zhang, X.; Liu, K.; Xiao, J. Q., Memory Effect in Magnetic Nanowire Arrays. *Adv. Mater.* **2011,** *23* (11), 1393.
61. Burks, E. C.; Gilbert, D. A.; Murray, P. D.; Flores, C.; Felter, T. E.; Charnvanichborikarn, S.; Kucheyev, S. O.; Colvin, J. D.; Yin, G.; Liu, K., 3D Nanomagnetism in Low Density Interconnected Nanowire Networks. *Nano Lett.* **2021,** *21*, 716−722.
62. Sung Lee, J.; Myung Cha, J.; Young Yoon, H.; Lee, J.-K.; Keun Kim, Y., Magnetic multi-granule nanoclusters: A model system that exhibits universal size effect of magnetic coercivity. *Scientific Reports* **2015,** *5* (1), 12135.
63. Baranowski, L. L.; Snyder, G. J.; Toberer, E. S., The misconception of maximum power and power factor in thermoelectrics. *J. Appl. Phys* **2014,** *115*, 126102.
64. Cheikh, D.; Bux, S. K.; Dunn, B. Synthesis and Characterization of Rare-Earth Tellurides and Their Composites For High-Temperature Thermoelectric Applications. UCLA, 2017.
65. Cerretti, G.; Villalpando, O.; Fleurial, J. P.; Bux, S. K., Improving electronic properties and mechanical stability of $Yb_{14}MnSb_{11}$ via W compositing. *J. Appl. Phys.* **2019,** *126* (17), 175102.
66. Cheikh, D.; Hogan, B. E.; Vo, T.; Von Allmen, P.; Lee, K.; Smiadak, D. M.; Zevalkink, A.; Dunn, B. S.; Fleurial, J.-P.; Bux, S. K., Praseodymium Telluride: A High-Temperature, High-ZT Thermoelectric Material. *Joule* **2018,** *2* (4), 698-709.
67. Gayner, C.; Amouyal, Y., Energy Filtering of Charge Carriers: Current Trends, Challenges, and Prospects for Thermoelectric Materials. *Advanced Functional Materials* **2019,** *30* (18), 1901789.
68. Pugh, E. M.; Rostoker, N., Hall Effect in Ferromagnetic Materials. *Rev. Mod. Phys.* **1953,** *25* (1), 151-157.
69. Snyder, G. J.; Ursell, T. S., Thermoelectric efficiency and compatibility. *Phys. Rev. Lett.* **2003,** *91* (14), 148301.

70. Snyder, G. J., Application of the compatibility factor to the design of segmented and cascaded thermoelectric generators. *Appl. Phys. Lett.* **2004,** *84* (13), 2436-2438.

For table of contents only:

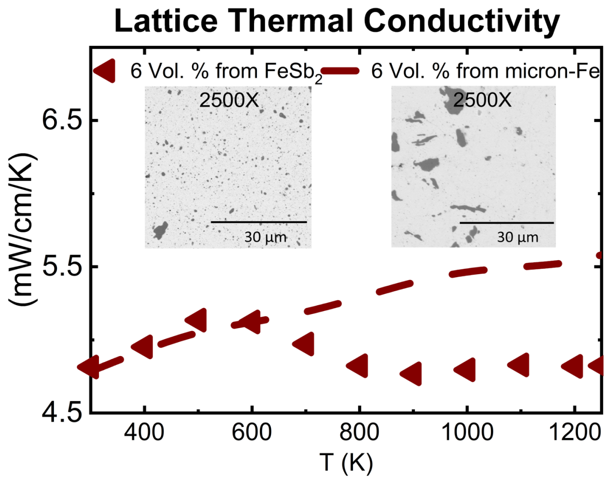

Synopsis:

$Yb_{14}MgSb_{11}$ composite with nanoscale iron is synthesized by employing a reactive precursor, $FeSb_2$ as the iron source producing nanosized well dispersed iron particles. The nanosized iron inclusions provides a reduction in lattice thermal conductivity and an overall 9 % improvement in *zT* at 1, 2, 3 Vol % compared to composites prepared with micron-size iron. $Yb_{14}MgSb_{11}$ with nanoscale iron composites maintain their *zT* up to 7.3 Vol % iron.